

15 GHz Monitoring of the Gravitational Lens MG 0414+0534

CHRISTOPHER B. MOORE¹ AND JACQUELINE N. HEWITT²
M.I.T. Department of Physics and Research Laboratory for Electronics

to appear in the Astrophysical Journal, November 1997

Abstract

We report the results of monitoring the four images of the gravitational lens MG 0414+0534 at 15 GHz. In 35 VLA maps spanning 180 days, we measure root-mean-square variations in the image light curves of $\sim 3.5\%$ mostly due to variations in the flux density calibration. The flux ratios, which are independent of flux density calibration variations, show root-mean-square variability of 1–3%. Extensive simulations of the data analysis process show that the observed variations in the flux ratios are likely to be due entirely to errors in the deconvolution process. It is possible that some of the observed variation is due to the source; however, the signal-to-noise ratio is too small to make a time delay determination using a data set of this size.

Subject headings: cosmology: observations - gravitational lensing -
quasars: individual (MG 0414+0534)

¹Current Address: Kapteyn Astronomical Institute, Postbus 800, 9700 AV Groningen, The Netherlands; cmoore@astro.rug.nl

²MIT Room 26-327, 77 Massachusetts Avenue, Cambridge, MA 02139; jhewitt@maggie.mit.edu

1 Introduction

Well before the first gravitational lens was discovered, Refsdal (1964a; 1964b) pointed out that, given a model of the lensing potential and the redshift of both the source and the lens, a measurement of the difference in optical path length between two images in a gravitational lens could be used to determine the Hubble parameter. More recently, Narayan (1991) has shown that a time delay measurement combined with a model of the lensing potential provides a measure of the angular diameter distance to the lens that is independent of the redshift of the source and cosmological assumptions other than local isotropy and homogeneity transverse to the line of sight. Thus, lens models combined with time delay measurements and lens redshifts can be used to measure the relationship between angular diameter distance and redshift. The measurement of the angular diameter distance–redshift relation at a variety of lens redshifts will allow the comparison of the measured relation to that predicted by cosmological models. Large-scale structure may contribute to the deflection and time delays in strong lensing (Seljak 1994; Bar-Kana 1996) raising the interesting possibility of detecting the effect of large-scale structure in a sample of lenses.

For a time delay measurement we have selected the gravitational lens MG 0414+0534, a source that was culled from the MIT–Greenbank survey (Bennett *et al.* 1986) in a gravitational lens search (Hewitt *et al.* 1988) and followed up with optical and radio observations. The object consists of four bright, highly reddened images with very similar radio spectra and optical colors. These characteristics, along with the morphology and relative brightnesses of the images, were taken as early evidence that the object is indeed a gravitational lens (Hewitt *et al.* 1992). Further study has supported that finding. Katz and Hewitt (1993) confirmed that the close double (components A1 and A2) is indeed a double as predicted by lens models. Optical (I-band) observations at the Michigan-Dartmouth-MIT observatory at Kitt Peak have detected the lensing galaxy at nearly the expected position (Schechter & Moore 1993). Spectroscopy by Angonin-Willaime *et al.* (1994) shows that the spectra of A1+A2 and B are similar. Infrared spectroscopy by Lawrence *et al.* (1995) suggests that the source is a fairly typical quasar that is highly reddened by dust in the lensing galaxy (but see Vanderriest *et al.* (1995) and Annis *et al.* (1993) for other views). A 15 GHz radio image of MG0414 is displayed in Figure 1.

MG0414 is well suited to relating time delay measurements to angular diameter distances since the morphology of the system argues for a relatively simple lensing potential (particularly compared to QSO B0957+561). Furthermore, HST, VLA, and VLBI studies of the object are underway which have revealed structure that may be used to place constraints on models of the lensing potential (Falco *et al.* 1997; Trotter Wilson 1997; Katz *et al.* 1997; Ellithorpe 1995; Patnaik & Porcas 1995).

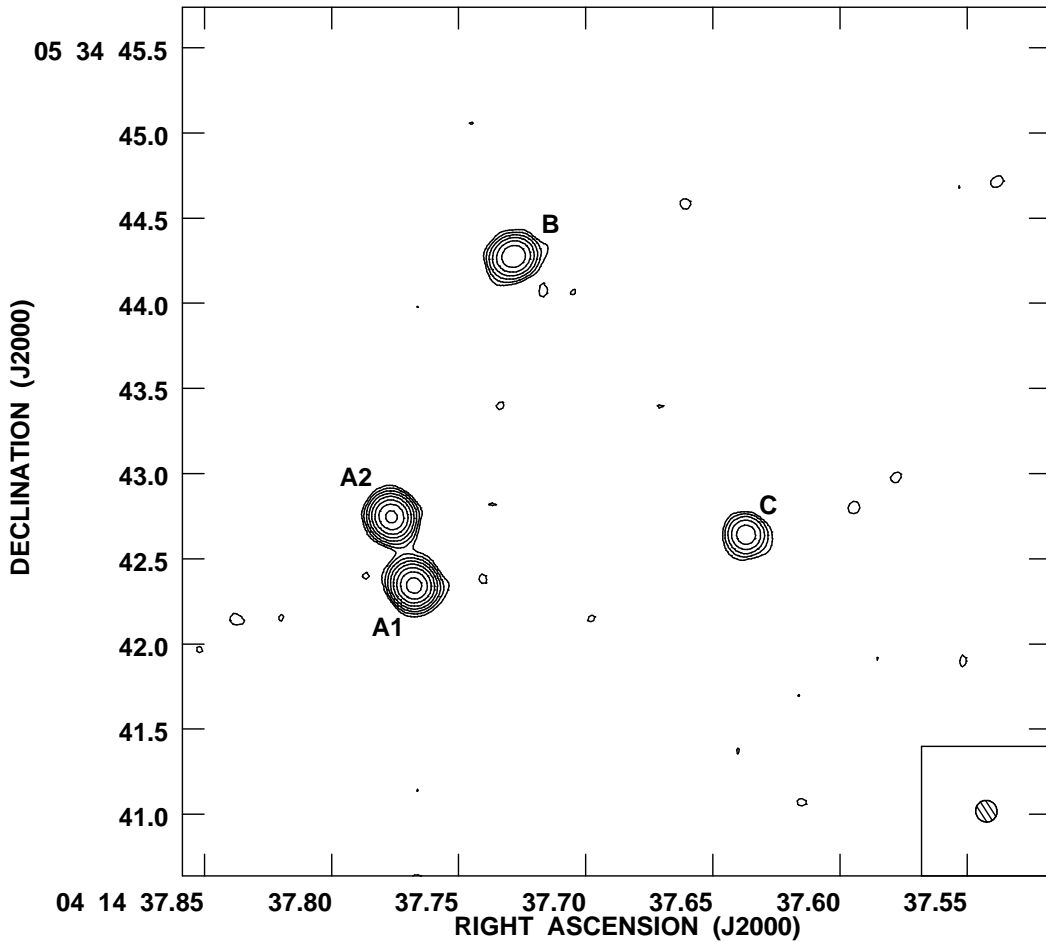


FIGURE 1: A 15 GHz (A-array) map of MG0414 produced in the course of the present work (observation date 15 Dec 1992). The contours correspond to flux densities of 0.8, 1.6, 3.2, 6.4, 12.8, 25.6, 51.2, and 102.4 mJy. The circle in the lower right corner illustrates the size of the synthesized beam for this observation ($.15'' \times .14''$).

1.1 Lens Models

Kochanek (1991) has fit five simple models of the lensing potential in MG0414 using *only* the positions of the images as constraints for reasons of computational speed and lack of reliable data on the flux ratios. The models fall into two classes: those in which image B is at a minimum of the time delay surface (models 2, 3, and 4) and those in which it is at a saddle point (models 1 and 5). In order to illustrate the difference between the two classes of models we show Kochanek's model 1 (Sin-

gular Isothermal Sphere + Internal Quadrupole) and model 3 (Singular Isothermal Sphere + External Quadrupole). Since Kochanek does not publish the fitted source positions, we estimate the source position by computing the source position implied by each observed image. Images A1, A2, and B give consistent estimates of the source position and we take their average as our estimate ($0.053''$, $-0.050''$ from the lens center for model 1 and $-0.13''$, $0.046''$ for model 3). Figure 2 shows the lensing potentials for both models (from Kochanek's fits) and our estimated source position. Even though the position angles of the potentials differ by approximately 90° , the

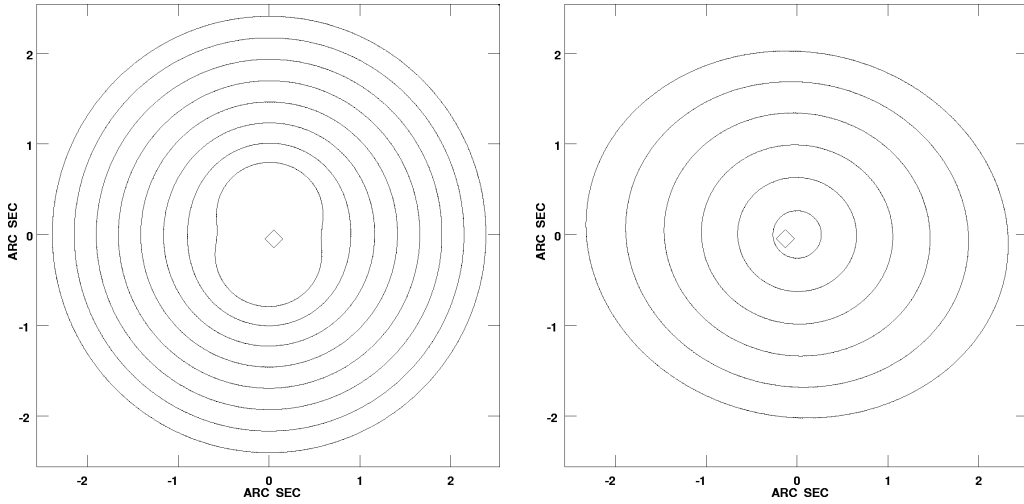


FIGURE 2: The gravitational potential for Kochanek's model 1 (left) and model 3 (right). The contours are equipotentials which are equivalent (in the weak field limit) to lines of constant index of refraction. The diamond signifies our estimated source position. The central detail in model 1 has been suppressed in order to make the source position visible.

radial deflections and therefore the Einstein rings generated by these models are nearly aligned.

Figure 3 displays the time delay surfaces corresponding to the two models. By the Fermat principle, images are formed at the extrema (marked) of the time delay surface. Both models can reproduce the positions of the images, but they do so very differently: saddle points and minima are exchanged in the two time delay surfaces. The B:C flux ratio predicted by Kochanek's models 1 and 5 (.58 and .51 respectively) is inconsistent with our observations where the measured flux ratio is 2.53. Models 2, 3, and 4 come closer to the measured B:C flux ratio (2.2–3.2) but fail to correctly predict the A1:A2 flux ratio. The very large magnification gradient in the neighborhood of A1 and A2 should make the flux ratio of A1:A2 difficult to

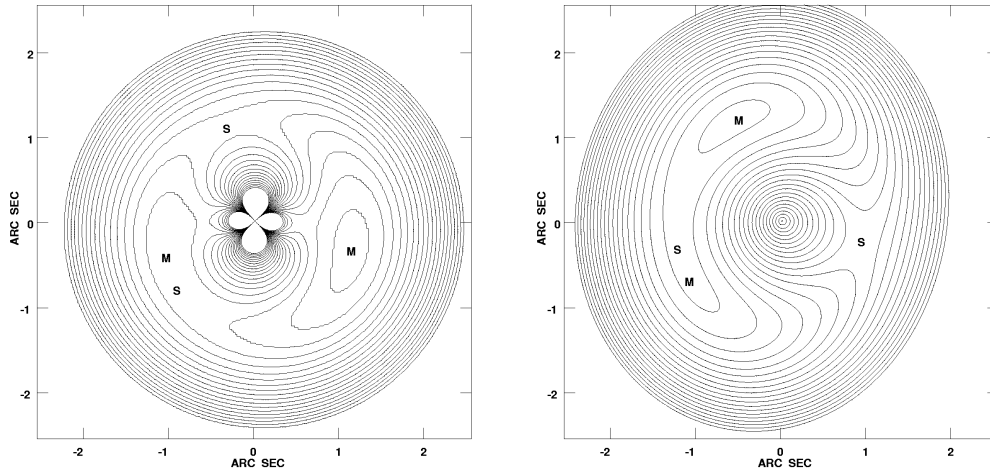


FIGURE 3: The time delay surface for Kochanek’s model 1(left) and model 3(right) using the assumed source positions shown in Figure 2. Extrema (with the exception of the central maximum) are labelled “M” for minimum and “S” for saddle point.

model.

The models that are consistent with the measured flux ratios predict that flux variations should be observed first in image B, following next in A1 & A2, and finally in image C. The model of the system by Hewitt *et al.* (1992) predicts (for $H_0 = 80 \text{ km s}^{-1} \text{ Mpc}^{-1}$, $q_0 = 0.5$, empty beam) that images B and A2 lead A1 by 12 and 0.3 days respectively and that image C lags A1 by 19 days. It should be noted that the model upon which these estimates are based should be taken to be illustrative only since it assumes a lens redshift ($z_l = 0.47$) and does not exactly reproduce the observed geometry and flux ratios of the system.

2 Observations

We observed MG0414 at 15 GHz with the Very Large Array³ (VLA) starting on 1992 November 8 in its most extended (A-array) configuration, continuing through the second most extended (B-array) configuration, and ending on 1993 May 3. The central frequencies for the two observing bands were the standard VLA U-band values of 14.9649 and 14.9149 GHz, each with 50 MHz bandwidth. Each band was observed in both senses of circular polarization bringing the total observed bandwidth to 100 MHz in each polarization. There were a total of 63 individual observations

³The VLA is part of the National Radio Astronomy Observatory, which is operated by Associated Universities, Inc., under cooperative agreement with the National Science Foundation.

each of 0.5 to 1.5 hours duration. The total time spanned by the observing program and the sampling interval of the observations were chosen so that for a reasonable range of the (unknown) lens redshift, at least one delay would be detectable. This program was scheduled into small interstices in the VLA schedule resulting in obser-

Date	Julian Date -244000.0	Source Elevation (degrees)	Synthesized Beam (")	Date	Julian Date -244000.0	Source Elevation (degrees)	Synthesized Beam (")
1992 NOV 02	8928.674	13-19	.35 × .23	1993 FEB 01	No Data		
NOV 03	No Data			FEB 03	9021.685	50-52	.48 × .24
NOV 04	8930.997	28-34	.27 × .25	FEB 06	9024.677	50-52	.50 × .30
NOV 07	No Data	60-62	.16 × .13	FEB 09	9027.690	40-44	.58 × .26
NOV 13	8939.772	47-50	.15 × .13	FEB 12	9030.533	50-52	.45 × .23
NOV 14	8940.894	53-55	.15 × .13	FEB 14	9032.665	40-48	.53 × .38
NOV 18	8944.738	50-52	.16 × .15	FEB 15	9033.673	40-44	.59 × .40
NOV 23	8949.744	47-50	.22 × .22	FEB 18	9036.707	29-34	.56 × .50
NOV 24	8950.971	22-26	.33 × .20	FEB 19	9037.522	50-54	.72 × .33
NOV 25	8951.864	53-55	.16 × .14	FEB 23	9041.704	23-33	.39 × .39
NOV 26	8952.692	37-41	.15 × .15	FEB 27	9045.661	35-39	.43 × .37
NOV 27	8953.963	25-28	.32 × .20	MAR 05	9052.473	50-52	.40 × .39
NOV 29	8955.707	50-52	.15 × .13	MAR 09	9056.357	29-34	.69 × .67
NOV 30	8956.850	53-55	.16 × .14	MAR 15	9062.474	52-55	.39 × .32
DEC 03	8959.754	52-54	.17 × .17	MAR 18	9065.501	54-55	.41 × .33
DEC 07	No Data			MAR 24	9070.575	40-44	.38 × .35
DEC 13	8969.814	48-50	.16 × .14	MAR 31	9077.535	44-48	.43 × .35
DEC 15	8971.845	43-48	.15 × .14	APR 01	9078.539	40-48	.45 × .35
DEC 16	8972.617	32-36	.14 × .14	APR 03	9081.334	34-41	.45 × .35
DEC 24	8980.533	20-24	.35 × .22	APR 05	9083.476	52-54	.38 × .33
DEC 27	8983.673	51-53	.17 × .14	APR 06	9084.494	49-52	.37 × .33
DEC 29	8985.602	37-41	.14 × .14	APR 11	9089.516	40-44	.44 × .35
1993 JAN 04	8991.671	53-54	.16 × .14	APR 12	9090.499	45-48	.37 × .34
JAN 06	8993.634	49-53	.17 × .14	APR 15	9093.491	45-48	.39 × .34
JAN 07	8994.699	54-55	.17 × .15	APR 19	9097.417	54-55	.38 × .34
JAN 11	8999.514	23-30	.27 × .22	APR 20	9098.498	44-48	.35 × .33
JAN 16	No Data			APR 22	9100.493	40-44	.38 × .34
JAN 19	No Data			APR 24	9102.343	58-59	.43 × .39
JAN 21	9008.704	49-51	.16 × .14	APR 27	9105.315	47-49	.38 × .34
JAN 24	9011.607	60-61	.17 × .16	APR 29	9107.286	48-52	.41 × .35
JAN 30	9017.614	54-55	.42 × .25	MAY 01	9109.247	29-40	.36 × .34
				MAY 03	9111.378	54-55	.41 × .32

TABLE 1: Journal of Observations

ervations occurring over a wide range of hour angle and with no particular sampling pattern (see Table 1). We have found that, in practice, an irregular sampling pattern is desirable because it minimizes windowing effects in the time delay analysis.

Some of the observations took place when the source was at very low elevation. These data are problematic since the projection of the baselines of the array and the resulting large synthesized beam makes deconvolution difficult, and because the atmospheric contribution to phase errors and flux calibration errors is much larger.

3 Data Reduction

The data were reduced using the National Radio Astronomy Observatory’s Astronomical Image Processing System (AIPS). After the initial excision of raw data that were clearly corrupted by interference or hardware problems, all data sets were processed by AIPS with a “run file” that applied the same processing to each observation. Complex antenna gains were determined by observations of J0423-013.

Refined estimates of the antenna phases were obtained by self-calibration (Cornwell & Fomalont 1989). Observations of 3C 48 were used to set the flux density scale but in order to use as many of the available baselines as possible, we used a model of the source based on four minutes of A-array observation kindly provided by C. Katz.

We used the CLEAN (Högbom 1974) algorithm implemented within the AIPS task MX (Clark 1980; Schwab 1984) to deconvolve each image. CLEAN is an iterative procedure that, for each iteration, selects the brightest pixel in the map and subtracts a fraction of it multiplied by the dirty beam. As a result, when two point sources are very close together, components tend to fall spuriously between them. This effect becomes particularly troublesome for the B-array data in which the A1–A2 doublet is barely resolved. Our initial attempts to clean these data resulted in a single bright source located between the two images with flux extending from the center towards the true image positions. When we instead used the knowledge of the relative positions of the components as measured from our A-array maps to constrain CLEAN so that it only attempted to place clean components in $0.12''$ square boxes centered on each component, we found that the quality of the deconvolution improved as evidenced by comparison of the B-array maps to the A-array maps.

When two point sources are barely resolved it is difficult to measure their flux densities independently. We attempted to use the AIPS task JMFIT to fit two gaussians to the A1–A2 double and found a strong covariance between the measured flux densities. Since we have already fitted for the flux densities of each component in the image deconvolution step, we instead measure the flux density of each image by summing the flux density of the CLEAN components in the box centered at the image position. This CLEAN flux density does not reliably measure the total flux density when the clean components do not reliably represent the total flux distribution (e.g. for extended sources). Since all four images in MG0414 are nearly point-like, the CLEAN components contain essentially all of the flux and can be used directly to get the flux densities. Our flux density measurement was compared to the results of JMFIT by creating artificial data sets with the same uv -sampling as typical data and four gaussian components with parameters measured from our A-array images. Gaussian white noise was added to all visibilities so that the noise in the image was comparable to the noise measured in the real images. The artificial data sets were deconvolved in exactly the same way as the real data and the resulting images then measured with JMFIT and by our technique. The results are comparable for the case when all images are well resolved (A-array) but in the B-array data, the A1–A2 pair is marginally resolved and our flux densities for those images had a variance smaller than those of JMFIT by a factor of ~ 50 .

Weather conditions can make flux calibration at 15 GHz very difficult. The most important effects are varying absorption due to the proximity to the water absorption line at 22 GHz and wind-induced pointing errors of the individual array antennae. For example, we have measured variations in calibrator flux density of a factor of ~ 1.5 over a period of 25 minutes at the beginning of a snowstorm. (The

data from that particular observation are omitted from our analysis.) Since flux calibration errors can substantially affect the results of the analyses to be discussed below, these analyses are carried out using only those observations made when the wind speed was less than 10 m/s, the object was above 30° elevation, there was no precipitation, and the phase stability of the atmosphere allowed reliable calibration of the complex antenna gains. Of the original 63 observations, three were lost to equipment failures at the VLA site, calibrations for two were lost to human error at operations, and one was lost to snow filling the dishes. Of the remaining 57 observations, we exclude from analysis five for high wind, eight for precipitation, two for atmospheric phase instability, and seven for low elevation, leaving 35 observations. Table 2 lists the measured flux densities for all components for each of the 35 observations.

Julian Date	Flux Densities (mJy)				Julian Date	Flux Densities (mJy)			
	A1	A2	B	C		A1	A2	B	C
-2440000.0					-2440000.0				
8930.9968	153.8	134.6	59.8	22.6	9021.6846	154.0	137.0	59.0	22.9
8939.7717	163.7	146.0	66.1	22.9	9024.6766	151.4	134.6	58.4	22.1
8940.8936	153.2	135.8	59.2	22.6	9030.5334	156.7	139.1	59.0	22.4
8944.7380	161.7	142.2	63.7	23.1	9032.6650	151.8	136.5	57.7	22.6
8951.8637	148.4	131.3	58.3	21.7	9036.7067	155.1	137.1	58.8	22.6
8952.6917	158.0	139.7	60.5	23.4	9045.6612	157.7	138.8	59.6	23.1
8955.7073	160.8	140.8	62.7	23.3	9052.4733	154.1	133.8	58.9	20.9
8956.8501	152.7	136.6	60.0	22.9	9070.5746	159.6	140.0	59.6	23.4
8959.7535	147.6	130.5	58.2	21.4	9077.5345	162.4	145.0	61.0	23.7
8971.8451	150.8	132.7	58.3	22.5	9078.5392	160.3	143.0	61.3	22.9
8983.6726	150.8	133.9	59.4	22.0	9081.3337	149.4	129.9	55.1	21.4
8991.6712	149.6	133.0	57.3	22.3	9083.4761	144.5	127.0	54.2	20.7
8993.6338	163.8	145.5	62.8	24.4	9093.4906	152.1	132.8	56.9	21.5
8994.6986	148.8	131.7	57.7	22.2	9098.4980	152.5	133.3	56.8	21.9
9008.7038	148.1	132.9	57.0	21.1	9100.4928	158.8	139.4	59.2	23.5
9011.6065	146.9	130.4	58.8	22.0	9105.3149	155.1	139.2	60.5	22.7
9017.6137	151.5	133.8	57.6	22.0	9107.2857	156.1	137.2	59.7	22.8
					9111.3782	149.2	131.7	56.8	22.1

TABLE 2: Table of measured flux densities (in mJy).

Figure 4 displays the measured light curves for all four images in MG0414. The variability is still clearly dominated by the flux calibration errors caused by variable atmospheric water content, differences in source and calibrator elevations, flux calibrator modelling errors, and weather conditions. Even with these effects, the RMS variability in the resulting four light curves (without any adjustment for possible source variability) is only 3.3–3.9%. Since this includes both source variability and flux calibration errors, the relative flux calibration is at least this good over the

whole data set.

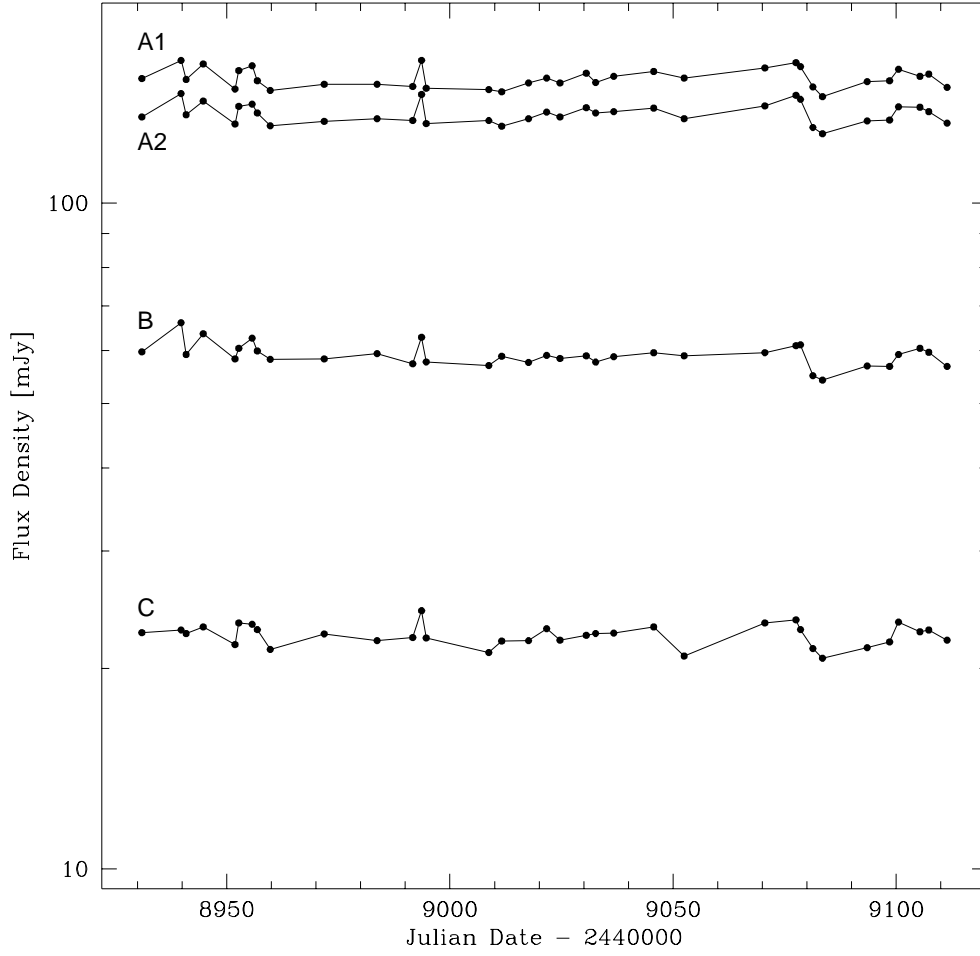


FIGURE 4: Light curves for all components shown on a log scale so that shifting on the vertical axis is equivalent to scaling.

4 Analysis

4.1 Variability in the Source

Source variability is prerequisite to the determination of a time delay but the uncertainties in the flux calibration obscure any evidence for source variability in the light curves of Figure 4. In order to determine if there is source variability, we compare the variations in the ratios of various images. Figure 5 displays “ratio light curves” in which the flux density of each component is normalized to component B. For

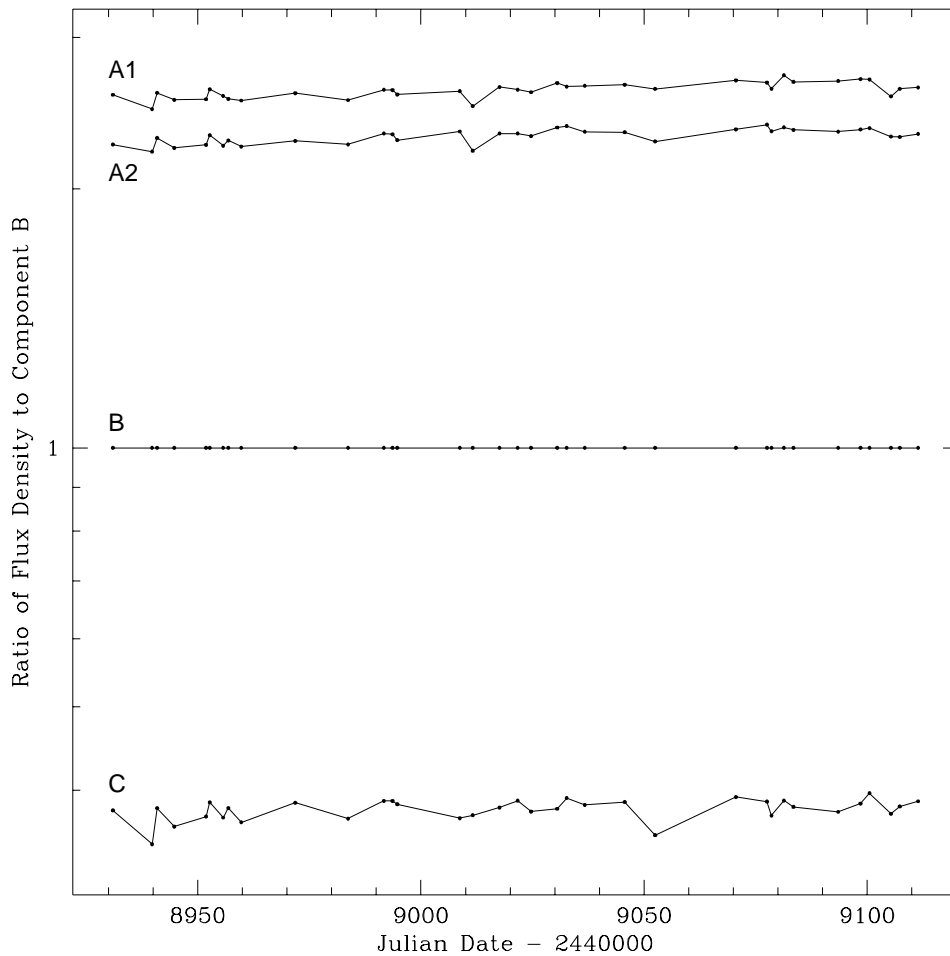


FIGURE 5: Time history of the ratio of the flux density of each image to image B. Shown on a log scale so that shifting on the vertical axis is equivalent to scaling.

comparison, we generated an artificial data set with the same uv -sampling as the real data, the average fluxes for the four components of MG0414 that we measure, and no source variability (created by the AIPS task UVMOD). An estimate of the RMS noise (per visibility) was obtained from the phase calibrator observations in the real data and gaussian noise of this amplitude was added to the visibilities in the artificial data. This complete artificial data set was then processed with the same run-file as the real data. Table 3 displays the RMS variability in each flux ratio for both the real data and the artificial data described above. These results demonstrate that uncertainties in the map computation and flux estimation procedures are comparable to the uncertainties in the calibration of the overall flux density scale. Thus, there is no evidence here that any source variability has been detected.

Ratio	Real Data	Artificial Data
A1:A2	0.9%	1.4%
A1:B	2.1%	1.9%
A2:B	1.9%	1.4%
A1:C	2.2%	2.6%
A2:C	2.1%	2.8%
B:C	2.9%	2.7%

TABLE 3: Measured RMS variability in image flux density ratios for the data reported here and an artificial data set with similar instrumental properties.

Another measure of variability is the first order structure function (Simonetti *et al.* 1985),

$$V(\tau) = \frac{1}{2} \langle [s(t) - s(t + \tau)]^2 \rangle$$

where $s(t)$ is the image flux density at time t , τ is the difference in time between two observations, and $\langle \rangle$ indicates the average.) We fit the structure function of the log of the radio data in decibels (referenced to 1 Jy), adopting a structure function of the form

$$V(\tau) = C\tau^{1.0}.$$

We expect that the structure function of instrumental errors will be that of white noise, so we take the power law part of the structure function as an estimate of the maximum possible variability in the source and find

$$V(\tau) = (0.000139 \frac{\text{decibels}}{\text{day}})\tau.$$

This implies that the signal-to-noise ratio for a single measurement of a change in flux density on time scales of interest (~ 20 days) is at most ~ 0.3 .

4.2 Time Delays and Correlated Variability

The data presented above provide no evidence that we have detected variability in MG0414. However, it is possible that some of the variability in the data is due to the quasar and that such “real” variability would manifest itself as itself in the form of a correlation between flux density measurements separated by the lens time delay. To investigate this, we computed discrete correlation functions (Edelson & Krolik 1988) for pairs of our light curves. No evidence for correlations was found in this analysis.

A time delay detection technique with greater statistical efficiency than cross-correlation techniques has been developed by Press, Rybicki, and Hewitt (1992a; 1992b); see also (Rybicki & Press 1992). Here we examine their χ^2 statistic (hereafter PRH- χ^2). To apply their method, one assumes (or better, fits for) a flux ratio between two images and then, for each trial delay, creates a combined light curve that consists of the union of the two light curves with one of them shifted and scaled relative to the other. For each trial delay, we ask how likely (in a χ^2 sense) the combined light curve is to have originated from a process whose variability is described by the assumed structure function. We have performed Monte Carlo simulations by generating 500 trials using the sampling of the data from this work, the delays predicted by the Hewitt *et al.* (1992) models, the noise measured from the data (assumed to be white gaussian), and assuming the source variability to be generated by a gaussian process with the same structure function as that estimated from the data. For comparison, we also performed the same simulation assuming no gravitational lens (i.e. every image is an independent source of gaussian noise again with the same structure function as that estimated from the data but uncorrelated with the other images). Figure 6 displays a histogram of the absolute minimum of the PRH- χ^2 curve on the interval [-45,45] for every image pair in the presence of the modelled gravitational lens. The simulations show that given the quality and quantity of the available data and the small (if present) variability of the source, extraction of a time delay is not possible by this technique. Only 22–31% of the measurements are within ± 5 d of the simulated delay. However, it is clear that the technique is detecting the presence of correlated variability since the correlated simulations show 3–6 times more measurements within 5 d of the simulated delay than the uncorrelated (no gravitational lens) simulations.

Even given the low signal-to-noise ratio of the present data, the PRH- χ^2 method is interesting since it uses all available lag pairs and is thus a very sensitive way to measure correlated variability. Given sufficiently large data sets, one can expect to detect correlated variability even when the signal-to-noise ratio for a single lag pair is less than unity (Hewitt *et al.* 1995).

From the measured MG0414 data, one can compute a distinct PRH- χ^2 curve for every pair of images using the average flux ratio as an estimate of the true flux ratio. The six curves computed from the present data are displayed in Figure 7. It is clear from examining the PRH- χ^2 curves that there is a strong correlation between

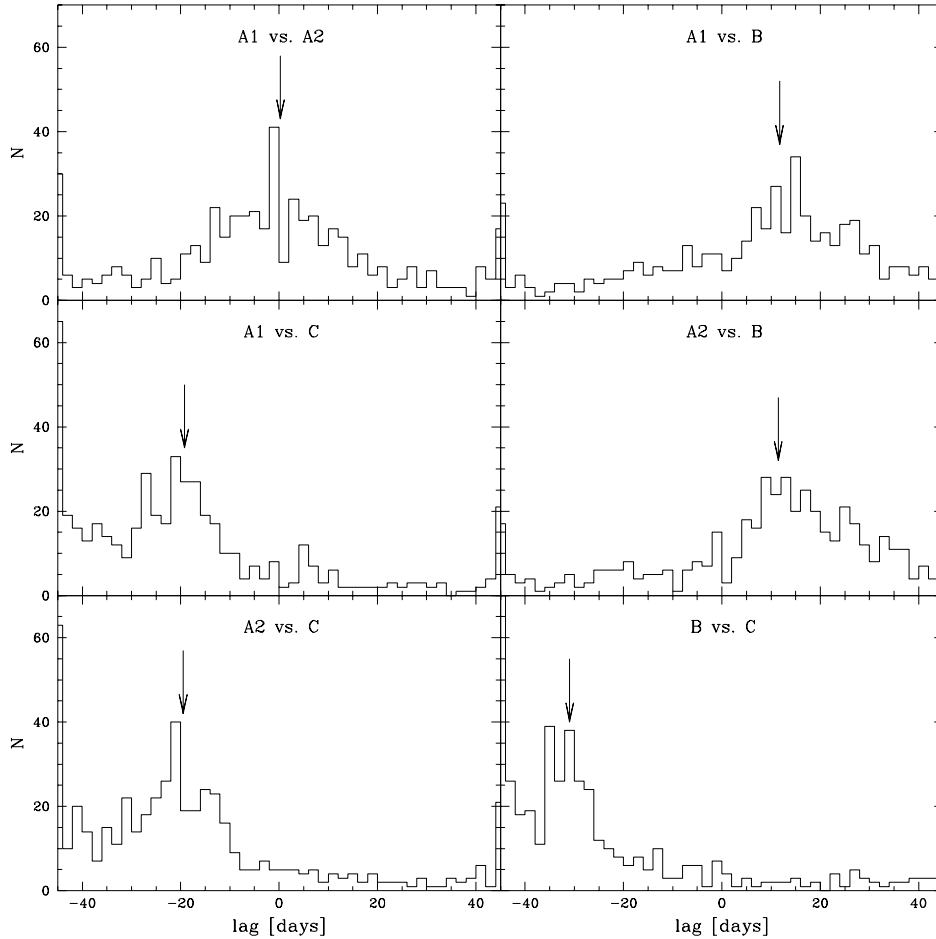


FIGURE 6: Histograms of the absolute minimum of the $\text{PRH}-\chi^2$ on the interval $[-45, 45]$ for 500 Monte Carlo trials assuming the presence of a gravitational lens. The model delay is marked with an arrow in each case. The bin on the left edge of the B vs. C plot is off-scale, its value is 121.

the light curves at zero lag due to unmodelled errors in the absolute flux calibration and that none of them presents a convincing argument for any particular time delay. This is not surprising. The signal-to-noise ratio of 0.3 for the variability as measured in a single lag pair (see Section 4.1 above) can be compared to the case of Hewitt *et al.*'s(1995) MG1131+0456 data for which the same ratio is 0.7. Their simulations

of time delay observations in MG1131 show that 50 to 100 flux measurements are required for a measurement of the time delay. Clearly this study of MG0414 suffers because there are too few measured points, given the small signal-to-noise ratio. It is interesting to note that in the cases where the PRH- χ^2 curves show a particular preference for the *sign* of the delay, it is consistent with the predictions of Kochanek's models 2, 3, and 4 (Kochanek 1991) and the Hewitt *et al.* (1992) model.

5 Conclusions

Measurement of a time delay from these data is difficult at best because the variability is very small, the small size of the data set gives few lag pairs, and the zero lag correlation caused by errors in flux calibration dominates the PRH- χ^2 curves. One could, in principle, modify the statistical model of the data used in the χ^2 analysis to account for the zero-lag correlation of the flux density calibration errors. However, given the limited expectation of a determination of a time delay we postpone such analysis until a better data set is available. Our current analysis does not provide a convincing case for source variability or for any particular value of a time delay in MG0414.

Improved experiments for measuring this time delay might use one or more of the following strategies: obtaining a larger data set, observing at a lower frequency where flux calibration is more precise, or (conversely) observing at a higher frequency where the source is more likely to be strongly variable.

6 Acknowledgements

We gratefully acknowledge useful advice and comments from E.W. Bertschinger, R.A. Perley, S.R. Conner, R.C. Walker, W.H. Press, and D. Wunker. The observations described herein were greatly assisted by the efforts of the VLA staff. This work was supported by a David and Lucile Packard Fellowship in Science and Engineering, a National Science Foundation Presidential Young Investigator Award, and the M.I.T. Class of 1948.

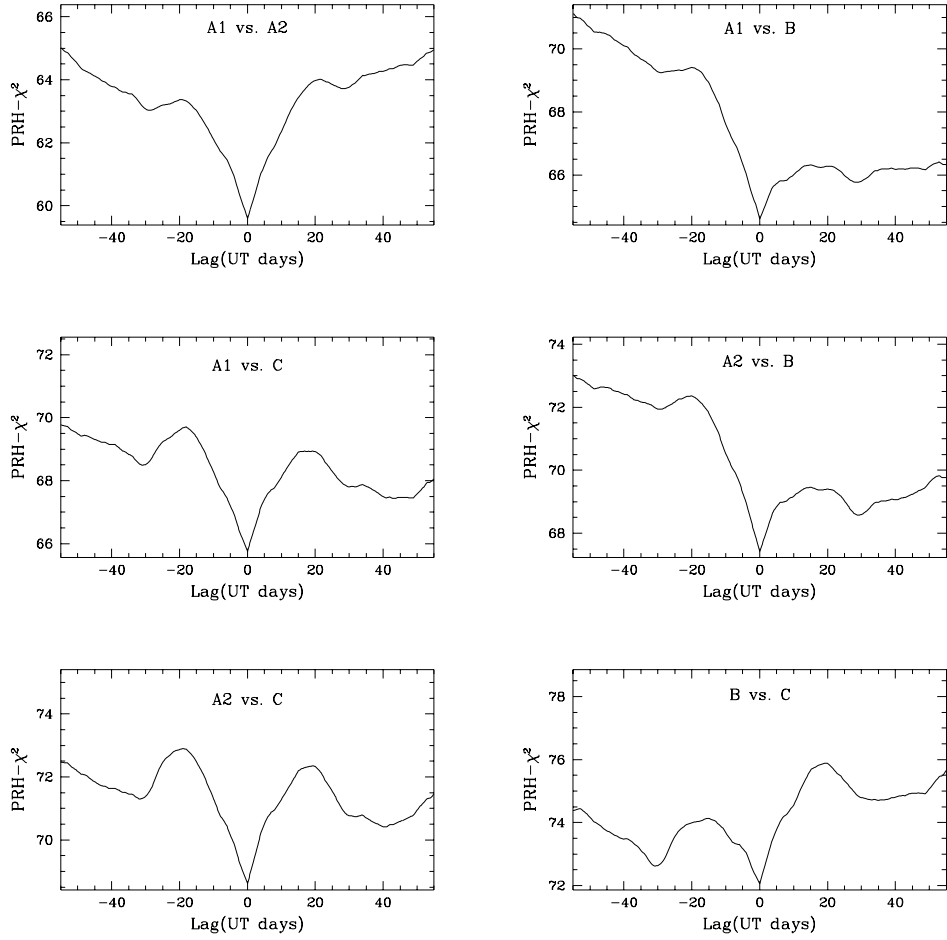


FIGURE 7: PRH- χ^2 curves for all pairs of components (69 degrees of freedom). Note the prominent feature at zero lag due to flux calibration errors. Also note that some of the curves, particularly those in the right column exhibit a strong preference for a particular *sign* of the delay. For ease of comparison, the curves are all plotted with the same vertical scale.

References

- Angonin-Willaime, M., Vanderriest, C., Hammer, F., & Magain, P., 1994, *A&A* **281**, 388
- Annis, J. & Luppino, G. A., 1993, *ApJ* **407**, L69
- Bar-Kana, R., 1996, *ApJ* **468**, 17
- Bennett, C. L., Lawrence, C. R., Burke, B. F., Hewitt, J. N., & Mahoney, J., 1986, *ApJS* **61**, 1
- Clark, B., 1980, *A&A* **89**, 377
- Cornwell, T. & Fomalont, E. B., 1989, in R. A. Perley, F. R. Schwab, & A. H. Bridle (eds.), *Synthesis Imaging in Radio Astronomy*, No. 6 in Conference Series, pp 185–197, Astronomical Society of the Pacific
- Edelson, R. & Krolik, J., 1988, *ApJ* **333**, 646
- Ellithorpe, J. D., 1995, *Ph.D. thesis*, M.I.T.
- Falco, E. E., Lehar, J., & Shapiro, I. I., 1997, *AJ* **113**, 540
- Hewitt, J., Burke, B., Turner, E., Schneider, D., Lawrence, C., Langston, G., & Brody, J., 1988, in J. Moran, J. Hewitt, & K. Lo (eds.), *Gravitational Lenses: Proceedings, Cambridge, Massachusetts, USA 1988*, No. 330 in Lecture Notes in Physics, pp 147–158, Springer-Verlag
- Hewitt, J., Turner, E., Lawrence, C., Schneider, D., & Brody, J., 1992, *ApJ* **104**, 968
- Hewitt, J. N., Chen, G. H., & Messier, M. D., 1995, *AJ* **109**, 1956
- Högbom, J., 1974, *ApJS* **15**, 417
- Katz, C. & Hewitt, J., 1993, *ApJ* **409**, L9
- Katz, C., Moore, C., & Hewitt, J., 1997, *ApJ* **475**, 512
- Kochanek, C., 1991, *ApJ* **373**, 354
- Lawrence, C., Elston, R., Jannuzi, B., & Turner, E., 1995, *AJ* **110**, 2570
- Narayan, R., 1991, *ApJ* **378**, L5
- Patnaik, A. R. & Porcas, R. W., 1995, in C. Kochanek & J. Hewitt (eds.), *Astrophysical Applications of Gravitational Lensing: Proceedings of 173rd Symposium of the IAU*, p. 305, Kluwer
- Press, W. H., Rybicki, G. B., & Hewitt, J. N., 1992b, *ApJ* **385**, 404
- Press, W. H., Rybicki, G. B., & Hewitt, J. N., 1992a, *ApJ* **385**, 416
- Refsdal, S., 1964a, *MNRAS* **128**, 295
- Refsdal, S., 1964b, *MNRAS* **128**, 307
- Rybicki, G. B. & Press, W. H., 1992, *ApJ* **398**, 169
- Schechter, P. L. & Moore, C. B., 1993, *AJ* **105**, 1
- Schwab, F., 1984, *AJ* **89**, 1076
- Seljak, U., 1994, *ApJ* **436**, 509
- Simonetti, J., Cordes, J., & Heeschen, D., 1985, *ApJ* **296**, 46
- Trotter Wilson, C. S., 1997, *M.I.T. Ph.D. thesis*, in preparation
- Vanderriest, C., Angonin-Willaime, M., & Rigaut, F., 1995, in C. Kochanek & J.

Hewitt (eds.), *Astrophysical Applications of Gravitational Lensing: Proceedings of 173rd Symposium of the IAU*, Kluwer